Boundary-Layer Meteorol (2018) 166:83–111
https://doi.org/10.1007/s10546-017-0292-8

RESEARCH ARTICLE

Effects of Explicit Urban-Canopy Representation on Local Circulations Above a Tropical Mega-City

José L. Flores Rojas[1] · **Augusto J. Pereira Filho**[1] · **Hugo A. Karam**[2] · **Felipe Vemado**[1] · **Valéry Masson**[3]

Received: 23 June 2016 / Accepted: 8 August 2017 / Published online: 24 August 2017

Abstract The Advanced Regional Prediction System (ARPS) is coupled with the tropical town energy budget (tTEB) scheme to analyze the effects of the urban canopy circulation over the metropolitan area of São Paulo and its interactions with the sea breeze and mountain-valley circulation in the eastern state of São Paulo, Brazil. Two experiments are carried out for the typical sea-breeze event occurring on 22 August 2014 under weak synoptic forcing and clear-sky conditions: (a) a control run with the default semi-desert surface parametrization and; (b) a tTEB run for the urban canopy of São Paulo. A realistic land-use database over the south-eastern domain of Brazil is used in the downscaling simulation to a horizontal grid resolution of 3 km. Our results indicate that ARPS effectively simulates features of the nighttime and early morning land-breeze circulation, which is affected by the surrounding hills and the nocturnal heat island of São Paulo. By early afternoon, the south-eastern sea-breeze circulation moves inland perpendicular to the upslope of the Serra do Mar scarp, which generates a line of moisture convergence and updrafts further inland. Later, the convergence

Electronic supplementary material The online version of this article (https://doi.org/10.1007/s10546-017-0292-8) contains supplementary material, which is available to authorized users.

✉ José L. Flores Rojas
joseflores@model.iag.usp.br

Augusto J. Pereira Filho
apereira@model.iag.usp.br

Hugo A. Karam
hugo@igeo.ufrj.br

Felipe Vemado
vemado@model.iag.usp.br

Valéry Masson
valery.masson@meteo.fr

1 USP/IAG/DCA, Universidade de São Paulo, São Paulo, Rua do Matão, 1226, São Paulo, SP, Brazil

2 UFRJ/IGEO/CCMN, Universidade Federal de Rio de Janeiro, Rio de Janeiro, Rua Athos da Silveira Ramos, 274, Bloco G1, Cidade Universitária - Ilha do Fundão Rio de Janeiro, Brazil

3 Centre National de Recherches Météorologiques, Météo-France/CNRS, Toulouse, France

line reaches São Paulo and interacts with the circulation arising from the urban heat island (UHI), which increases the moisture convergence and strength of updrafts. The surface energy balance indicates that the UHI is caused by large sensible heat storage within the urban canopy during the day, which is later released in the afternoon and at night. The simulations are verified with available radiosonde and surface weather station data, land-surface-temperature estimates from the moderate resolution imaging spectroradiometer, as well as the National Center for Atmospheric Research reanalysis databases. The three-dimensional geometry of the urban canyons within the tTEB scheme consistently improves the thermodynamically-induced circulation over São Paulo.

Keywords Urban boundary layer · Urban energy fluxes · Urban heat island · Sea-breeze circulation

1 Introduction

A sea breeze is a direct thermal circulation occurring near coastal areas from polar to equatorial regions, and develops during clear skies. As solar radiation heats the surface and the adjacent atmospheric boundary layer more rapidly over land than over sea, which results from the different heat capacities for land and water, the horizontal sea land temperature gradient induces a pressure gradient that forces a shallow layer of cooler and moist marine air to move inland (Simpson 1994). The governing features of a sea breeze are: (a) the diurnal cycle of the surface temperature, (b) heat diffusion, (c) atmospheric stability, (d) the Coriolis force, (e) the diffusion of momentum, (f) the topography and (g) the background flow. The first two are essential for the formation of the sea-breeze circulation, while the third is essential for its inland penetration.

The Coriolis force results in the change in direction of the sea-breeze flow over time and shortens its penetration inland (Simpson 1996). In mountainous areas, the front of the sea-breeze flow is intersected and channelled, which enhances flow convergence and updrafts. Furthermore, temperature advection increases the sea-breeze penetration (Innocentini 1981), while multiple sea-breeze fronts may collide and further strengthen updrafts (Melas et al. 2000). For Brazilian cities, Karam et al. (2003) used a single mass conservation model to estimate the horizontal flow over the complex topography of São Paulo and found agreement with observations. Therefore, the topography of São Paulo induces flow features characteristic of the surface.

Ribeiro et al. (2016) used a fully-coupled oceanic-atmospheric model to study the sources and sinks of turbulent kinetic energy (TKE) and the effects of topography and sea-breeze on the development of the planetary boundary layer (PBL) in the coastal area of Cabo Frio, Brazil. Their results indicate that both a lower sea-surface temperature (SST) as well as lower near-surface air temperatures are determined by coastal upwelling induced by strong wind speeds, leading to an intense temperature inversion, and, hence, a well-defined PBL.

Surface heterogeneities in urban areas modify atmospheric circulation by changing, for example, the momentum, latent and sensible heat fluxes, the boundary-layer height and surface-flow convergence. Moreover, optical properties are modified in urban environments (Synnefa et al. 2007; Ram et al. 2016), as well as in air pollution dispersion (Amorim et al. 2013; Moonena et al. 2013; Flores et al. 2016a), during thunderstorm initiation (Vemado and Pereira Filho 2016) and related physical and chemical processes. Urban centres are different from suburban regions in both material and geometry, with multiple intersecting paved roads, impervious surfaces and denser irregular constructions in urban areas. Such

differences modify the mass and energy budgets responsible for the urban heat-island (UHI) effect, with higher temperatures in its centre than the surroundings. Although the tropical and subtropical UHI effect is weaker than at higher latitudes, it is more intense in the summer daytime, because of the absorption of solar radiation by urban canopies (Amorim et al. 2013; Moonena et al. 2013; Flores et al. 2016a). However, the seasonal cycle is modulated by urban rural soil-moisture gradients (Pearlmutter et al. 2005; Heisler and Brazel 2010).

Flores et al. (2016b) estimated the surface UHI intensity, which is defined as the difference between urban and rural surface temperatures, for São Paulo and Rio de Janeiro cities using land-surface temperature (LST) data from the moderate-resolution imaging s pectroradiometer (MODIS) in combination with two methods: the first using a Gaussian surface to fit the difference between urban and rural patterns of LST (Streutker 2002), and the second based on statistical quantile analysis. For São Paulo, the diurnal maximum (minimum) surface intensity of the UHI is found to be 10.4 °C (4.6 °C) in November (July); for Rio de Janeiro, the diurnal maximum (minimum) surface intensity of the UHI is 7.9 °C (4.7 °C) in February (June).

While urban areas are able to be modelled with fine-grid mesoscale numerical models (Pielke et al. 1992; Dudhia and Bresch 2002; Xue et al. 2000a; Kusaka et al. 2001), the soil classification for urban areas in the range 0.5–2 km is unavailable in these studies. The studies of Urano et al. (1999) and Yamada (2000) developed the first schemes to handle urban boundary layers in mesoscale models. Chen et al. (2001) integrated several urban boundary-layer schemes into the Weather Research and Forecasting (WRF) model with the intention of bridging the gap between the mesoscale and microscale. Simulations for several metropolitan regions were realized to evaluate the sensitivity of urban parameters, the characterization of the UHI, boundary-layer profiles and urban plumes. Ganbat et al. (2015) investigated the interactions of the urban-breeze circulation with mountain-slope flow using the WRF model coupled with the urban-canopy model of the Seoul National University, and found an inverse relationship between the mountain height and urban fraction, and that the transition from an urban-side upslope flow to downslope flow occurs earlier.

Freitas et al. (2007) simulated the circulation over São Paulo in winter with the Regional Atmospheric Modeling System (Cotton et al. 2003) coupled with the town energy budget (TEB) scheme (Masson 2000), and showed that the UHI effect accelerates the incoming sea-breeze front towards the centre of São Paulo, with the induced circulation slowing the front of the sea breeze, leading to intense low-level convergence. In a similar approach, Oliveira de Souza et al. (2016) studied the urban evolution of Manaus City, Amazonas, and showed its effects on microclimate changes.

We use the Advanced Regional Prediction System (ARPS) to simulate explicit urban-canopy effects on the urban circulation to bridge mesoscale and microscale processes. The system provides a new formulation of urbanization impacts on several climate conditions and scenarios, which is used to analyze the interactions of the sea breeze with the mountain-valley and UHI circulation. A sea-breeze event in São Paulo on 22 August 2014 is simulated, as it is a typical winter event without deep convection.

Section 2.1 introduces the weather and climate features of São Paulo, while Sects. 2.2 and 2.3 describe the main features of ARPS and the urban parametrization, respectively, and their coupling is described in Sect. 3.1. The model configuration and experimental design are described in Sect. 3.2. A synoptic overview of the 22 August 22 2014 sea-breeze event is described in Sect. 4. The simulated and observed variables are analyzed in Sect. 5, and Sect. 6 gives conclusions.

2 Theoretical Elements

2.1 Site and Location

The metropolitan area of São Paulo is located in the south-eastern region of Brazil at 23°35′55″S, 46°37′46″W, at about 770 m a.s.l., and a distance of 60 km from the Atlantic Ocean. São Paulo is composed of 39 municipals, with a total population of 20 million inhabitants, or 11% of the population of Brazil, and is the largest industrial complex of South America. For instance, São Paulo City, which is the largest municipal, has had a growing population and increasing urbanization throughout the 20th Century, resulting in significant environmental impacts, with a higher air temperature by 2 °C, a lower relative humidity by 7% and a higher annual rainfall accumulation of 400 mm, among other changes (Pereira Filho et al. 2004). Floods and significant air pollution are among the major environmental impacts during the rainy season and winter, respectively.

São Paulo has a typical high-altitude tropical climate with two well-defined seasons: (1) a dry winter (June to August) and (2) a wet summer (December to February). August is the driest month, with an average precipitation of 35 mm, while January is the rainiest month, with an average precipitation of 255 mm (Pereira Filho et al. 2004). The relative humidity is highest between December and April.

The greater São Paulo region is under the influence of the South Atlantic anticyclone, which transports large amounts of moisture through the Amazon, as well as through southern and south-eastern Brazil. São Paulo is also influenced by polar fronts, bringing about drier and colder air throughout the year, especially in autumn and winter. North-west low-level jets transport moisture from the Amazon region to São Paulo, sometimes in association with the so-called South Atlantic convergence zone (Hidalgo Nunes et al. 2015), and bring widespread summer precipitation.

The surface-flow in São Paulo is north-west to south-easterly associated with the South Atlantic high-pressure system and the afternoon and early evening sea-breeze circulation shifting the wind direction from north-west to south-east, and increasing the surface wind speed (Fig. 6e). The sea-breeze front, which reaches São Paulo more than half the days of a year after passing the Serra do Mar ridge, injects the city with cool and moist air from the Atlantic Ocean. The intensity and penetration of the sea breeze have previously been related to the intensity of the UHI effect of São Paulo (Pereira Filho et al. 2004).

2.2 The Advance Regional Prediction System

ARPS is a fully-compressible three-dimensional model formulated in generalized terrain-following coordinates developed by the Center for Analysis and Prediction Storms of the University of Oklahoma (Xue et al. 2000b). The integration of the sound-wave containing equations is performed by a split-explicit scheme, which allows the efficient distribution of memory for massively-parallel processing by the horizontal domain-decomposition strategy (Xue et al. 2000b). Sound waves play a critical role in establishing mesoscale pressure gradients that drive the sea breeze (Miller et al. 2003).

ARPS includes modern physical parametrization schemes. For instance, the planetary boundary-layer and surface-layer parametrizations are used to evaluate the state of the land surface, which has a direct impact on the sensible and latent heat exchange with the atmosphere, as the soil-surface temperature and moisture content directly appear in the calculation of surface fluxes (Xue et al. 2001). In ARPS, the time-dependent state of the land surface is predicted by the equations of the surface energy and moisture budget based on the force-

restore scheme of Noilhan and Planton (1989) and Jacquemin and Noilhan (1990), which includes prognostic equations for: (a) both the temperature of the soil and vegetation, and (b) soil moisture using a two-layer force-restore algorithm. This scheme is designed to simulate the essential processes involved in surface-atmosphere interactions with the fewest parameters and complexities possible.

Numerical weather prediction is sensitive to the surface fluxes of heat, momentum and moisture. The ARPS has a stability and roughness-length dependent surface-flux scheme (Businger et al. 1971), and a procedure of Byun (1990) is used in the flux calculations to improve the efficiency with respect to the commonly-used iteration method. This procedure is based on the exact analytic solutions of Monin-Obukhov similarity theory (MOST), as well as stability parameters in terms of the gradient and bulk Richardson numbers for both stable and unstable atmospheric conditions. In addition, Businger's original formulation to estimate surface fluxes was further modified by Deardorff (1972b), so that the results are more realistic for both highly stable and unstable conditions.

Currently, as ARPS does not take into account the surface energy balance of urban canopies, analysis of the effects of urban energy fluxes on the interactions of local circulations requires the coupling of an urban energy budget scheme, such as the tTEB scheme described below.

2.3 The tTEB Scheme

The surface energy balance for the urban canopy used in mesoscale modelling can be classified into three categories: (a) empirical models; (b) vegetation models with or without drag-force terms adapted and modified for the urban canopy and; (c) urban-canopy models. Urban-canopy models accurately represent the three-dimensional nature of urban canopies by considering vertical and horizontal surfaces for improved representation of the specific energetics of the urban canopy (Masson 2006). Such schemes share the following characteristics: buildings have a three-dimensional shape, there are separate energy budgets for roofs, roads and walls, and radiative interactions between roads and walls are explicitly treated.

Urban canopy models can be divided into two categories: (1) parametrized canopy atmosphere or single-layer models where a single atmospheric layer interacts with the surface above the roof level; (2) drag approaches (Martilli et al. 2002) or multilayer models, where several atmospheric layers explicitly extend down to the canopy from the building level to the road. The simplest single-layer model is the TEB model (Masson 2000), which simulates turbulent fluxes of heat, momentum and mass into the atmosphere at the lower surface of the mesoscale atmospheric model composed of buildings, roads and other artificial materials. The TEB scheme parametrizes both the urban surface and the roughness sublayer. A constant flux is input to the atmospheric model, which damps daytime turbulent heat fluxes caused by the observed heat storage in urban areas.

The tTEB scheme (Karam et al. 2010) includes a broader range of surface characteristics with respect to the original TEB model (see Table 1): (a) the increased aerodynamic conductance for less stable conditions at the roughness sublayer; (b) a MOST formulation in the inertial sublayer; (c) a modified urban sub-surface drainage system to transport the intercepted rainfall by roofs to roads; (d) local scaling for flux-gradient relationships in the roughness sublayer; (e) multi-reflections of longwave radiation within the urban canyon (Arnfield and Mills 1994).

The framework of MOST with characteristic scales (Garratt 1980; Rotach 1995) is used to calculate turbulent fluxes in the surface layer under different stability conditions. The surface layer has a quasi-stationary constant flux over a horizontally homogeneous surface (Oke

Table 1 The main characteristics of the TEB (Masson 2000) and tTEB (Karam et al. 2010) schemes. Here, R_N is the net radiation flux, and Q_H is the sensible heat flux

Approach	TEB (Masson 2000)	tTEB (Karam et al. 2010)
Infrared irradiances	First-order reflections	Multiple reflections (Arnfield and Mills 1994)
Water budget	Infinite draining of the sub-surface ducts	Limited draining of sub-surface ducts (Grimmond and Oke 1991)
Sky-view factors	Noilhan (1981)	Oke (1987)
Free convection	Polynomial approach of free convection (Mascart et al. 1995)	Asymptotic behaviour of MOST (Grachev et al. 2000)
Urban-canyon temperature	Divergence of Q_H	Divergence of Q_H and R_N
Surface roughness and displacement	Constants (user defined)	Morphometric relations (Kastner-Klein and Rotach 2003)
Sensible heat flux	Modified flux-profile relation in the surface layer (Mascart et al. 1995)	Local scaling in the roughness sublayer and MOST in the inertial sublayer (Kastner-Klein and Rotach 2003)
Latent heat flux	As above	As above
Momentum flux	As above	As above

Table 2 Main ARPS-tTEB configuration

Category	Options
Governing equations	Three-dimensional, non-hydrostatic, compressible
Grid staggering	Logarithmic vertical stretching
Time differencing	Leapfrog and forward time differences
Turbulence closure	1.5-order turbulent closure
Upper boundary	Global Forecast System (resolution: 1°)
Lateral boundaries	Global Forecast System (resolution: 1°)
Mycrophysics	Schultz (1995) ice microphysical scheme
Cumulus parametrization	Kain and Fritsch (1993) scheme for the domain of 27 km
Radiation physics	Atmospheric radiation transfer parametrization
Surface physics	tTEB scheme for urban canopy and two-layer force-restore model for the vegetation canopy

1976). Since the urban surface layer is complex, it is divided into two sublayers (Rotach 1995): (a) the roughness sublayer where vertical turbulent fluxes are not constant, but generated by heterogeneous elements of the urban canopy (roads, houses, trees, etc.) and, (b) the inertial sublayer formulated by MOST is appropriate (Table 2).

Further details on turbulent energy fluxes in the inertial sublayer, in the roughness sublayer and the evolution of the water reservoir used in the tTEB scheme are to be found in Karam et al. (2010). Higher-resolution models down to 100 m explicitly represent certain urban areas. Thus, modelling of the urban canopy using the surface energy budget becomes necessary for

simulations with fully-compressible models. A step-by-step procedure to integrate ARPS is presented in Sect. 3.1.

3 Methodology

3.1 The Coupled System

Urban-canopy effects on atmospheric dynamics can be modelled with energy budget schemes coupled with compressible atmospheric models. Here, we present a step-by-step procedure for the integration of ARPS (Sect. 2.2) and the tTEB scheme (Sect. 2.3). Figure 1 shows a diagram with the main steps.

Firstly, variables in the tTEB scheme are transferred to the surface-physics module of ARPS, and secondly, ARPS dynamics and radiative variables are transferred to the tTEB scheme, where urban-type vegetation (semi-desert in the original ARPS) is located within the

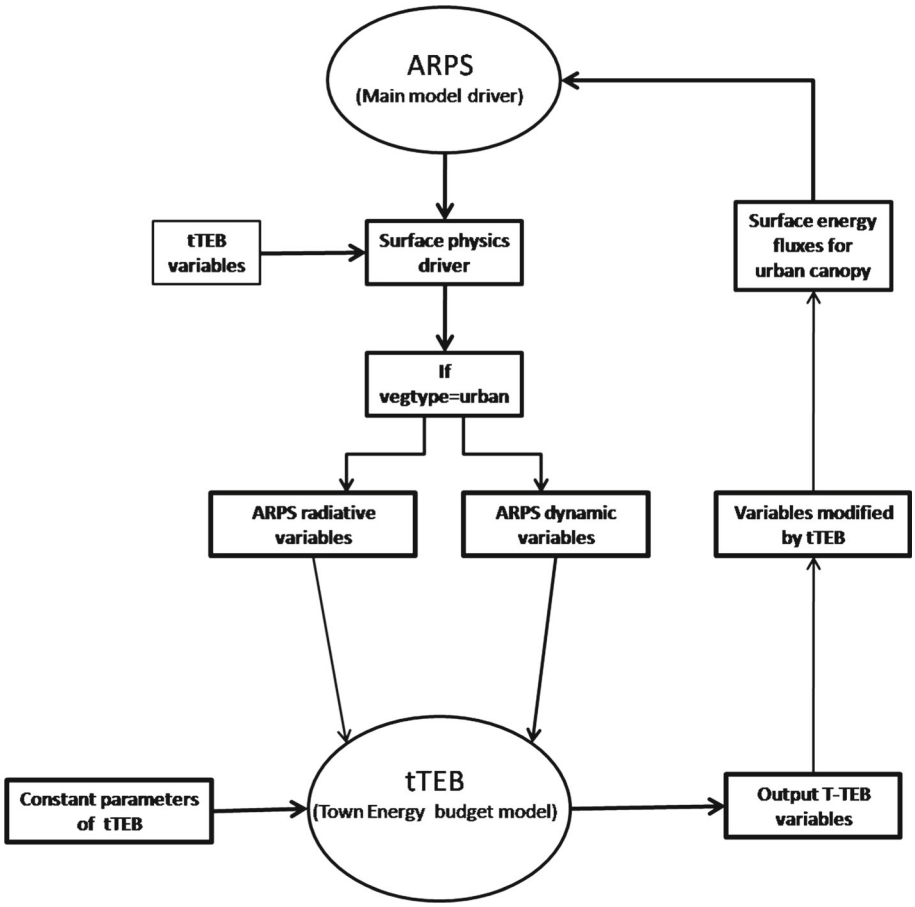

Fig. 1 Flow diagram of the integration of the tTEB scheme and ARPS. *Arrows* indicate the direction of variables and the transfer of parameters

model domain. Thirdly, the physical urban parameters of the tTEB scheme are set constant. Fourthly, the surface energy fluxes over the urban canopy are recalculated using surface variables modified by the output variables of the tTEB scheme. Finally, the urban energy fluxes are transferred to ARPS to complete the cycle.

Version 5.3.4 of ARPS uses global land-use data and global top-layer soil-type data from the U.S. Geological Survey at a 30-s resolution. These datasets are used by the surface subroutine of ARPS to derive soil features, such as the soil-type, vegetation type, the leaf area index and the roughness length.

The canyon surface temperature in the TEB scheme has three components: the substrate temperature, the external surface temperature and the canyon air temperature, while in the tTEB scheme, there are prognostic equations for the external temperatures at each surface (roofs, walls or roads) and a diagnostic equation for canyon temperature (Masson 2000). A soil temperature equation couples the output temperatures of roofs, walls and roads from the tTEB scheme with the surface temperature of ARPS, using

$$T_{surface} = a_{bld} T_{roof} + (1 - a_{bld}) T_{can}, \tag{1}$$

where T_{can} is the canyon temperature driven by entrainment of the urban boundary-layer air into the urban canopy, anthropogenic heat and humidity fluxes and the divergence of radiation (infrared) density flux through the surfaces of the urban canopy (Nunez and Oke 1976) [see Eq. 13 of Karam et al. (2010)]; T_{roof} is the roof surface temperature and a_{bld} is the fractional artificial area occupied by buildings. The tTEB scheme uses a variable draining ratio (Grimmond and Oke 1991) to estimate the time evolution of rainfall accumulation over roofs and roads. Surface variables, such as the soil water content and the surface specific humidity, are updated to couple ARPS with the tTEB scheme. The surface water content is modified by,

$$q_{surface} = a_{bld} q_{roof} + (1 - a_{bld}) q_{can}, \tag{2}$$

where q_{can} is the canyon air specific humidity that modifies the surface specific humidity q_{vsfc}, and is a function of the turbulent water vapour flux Q_E determined locally, and of the anthropogenic water vapour flux Q_{EA} released inside the urban canopy. In addition, q_{roof} is the roof-water moisture and a_{bld} is the fractional artificial area occupied by buildings.

Surface variables modified by the tTEB scheme ($T_{surface}$, $q_{surface}$) are updated each timestep, and the surface fluxes of heat, momentum and moisture are calculated using a stability and roughness-length-dependent surface-flux model using the modified Businger formulation (Businger et al. 1971). Traffic and industrial sensible and latent heat fluxes are added to the surface energy fluxes and then transferred to the land-surface sub-routine of ARPS. Moreover, the Kastner-Klein and Rotach (2003) morphometric relations drive the complex surface drag in atmospheric flow using the ratio between the building area A_p and city total area A_t and the height of the buildings to calculate the zero-plane displacement d and the roughness length z_0. The variation of z_0 and d with increasing building density is considered to provide a more realistic estimation than the other approximations. The configuration and experimental designs of the coupled system are described below.

3.2 Model Configuration and Experimental Design

The performance of the coupled system in simulating the effects of urban energy fluxes on local circulations in São Paulo is carried out with two realistic experiments for a typical sea-breeze event on 22 August 2014. The control experiment uses the original ARPS without any urban-canopy effects, but with a semi-desert canopy with biophysical parameters (see

Table 3 Biophysical parameters for three different types of vegetation cover in ARPS

Parameter class	Albedo	Emissivity	Leaf area index	Roughness length z_0 (m)	Zero-plane displacement d (m)
Grassland shrub cover	0.18	0.96	5	0.51	3.6
Grassland tree cover	0.2	0.95	6	0.06	0.7
Semi-desert (urban)	0.15	0.9	4.8	0.8	1.1

Table 4 Parameters of urban areas over São Paulo (Tarifa and Azevedo 2001) and the average values used in simulations with urban canopy

Parameter	Urban 1	Urban 2	Average
Building height (m)	50	5	10
Building aspect ratio (height/length)	2	1	1.2
Canyon aspect ratio (height/width)	3	0.5	0.9
Fractional area covered by artificial material	0.9	0.8	0.8
Fractional area covered by buildings	0.9	0.8	0.8
Traffic sensible heat release (W m^{-2})	30	20	21
Traffic latent heat release (W m^{-2})	7	5	5.3
Industrial sensible heat release (W m^{-2})	20	30	28.5
Industrial latent heat release (W m^{-2})	40	50	48.5

Table 3). The full experiment includes the effects of the urban scheme and urban-canopy parameters (Table 4).

Three nested horizontal grids at 27, 9 and 3 km are used within the domain at 23.54°S, 46.63°W (Fig. 2a). The 27-km grid domain has 143 × 143 points covering eastern South America and a 10-s timestep, while the same number of grid points are used for the 9-km and 3-km grids, but with a 6-s timestep. A 43-layer hyperbolic vertical grid is used, starting at 20 m (bottom) and increasing to a minimum resolution at an altitude of 20.5 km. The innermost domain corresponds to São Paulo. The vegetation cover at the 3-km grid is shown in Fig. 2b with semi-desert type set to 13, and topographic and atmospheric pressure fields over São Paulo are shown in Fig. 2c. The simulations were initialized for 1800 UTC, 21 August 2014, ending at 0000 UTC, 23 August 2014 (30 h).

Initial and boundary conditions for horizontally inhomogeneous initialization are obtained from the global forecast system, which is a global weather prediction system used by the US National Weather Service, containing a global numerical weather prediction model with variational analysis, generating data with a resolution up to 0.25° (Wang et al. 2013).

A 1.5-order TKE closure scheme is used for the subgrid boundary-layer turbulence (Xue et al. 2001). The Coriolis force and surface properties, with a sandy loam soil type and semi-desert vegetation cover, are used in the control and tTEB experiments. ARPS uses the Global Ecosystems Database, which adapts biophysical parameters, such as albedo and emissivity, displacement height, leaf area index, fractional coverage and roughness height, to the urban and vegetation canopies. The main land-use classes are semi-desert canopy (urban) within São Paulo, but otherwise grassland and deciduous forest (Fig. 2b); the biophysical parameters of the vegetation types are given in Table 3.

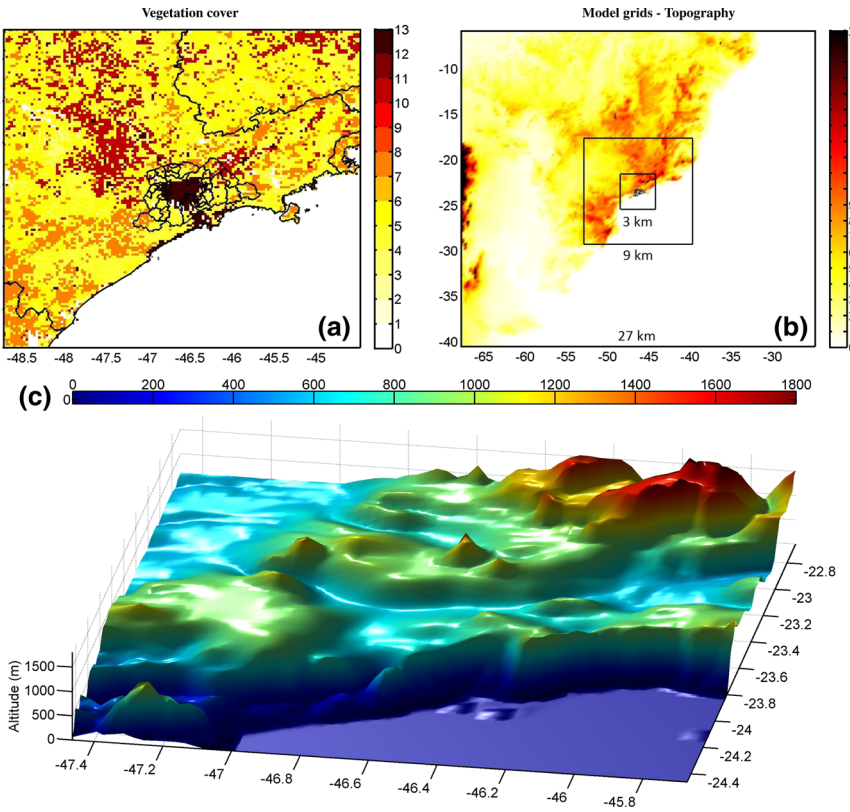

Fig. 2 **a** Vegetation types in ARPS for the 3-km domain with the urban canopy in *red*. **b** Simulation domains for the 27-km, 9-km and 3-km with the topography. **c** Three-dimensional view of the topography in the greater São Paulo area for the 3-km domain. Longitudes, latitudes, altitudes and geographical boundaries are indicated

For regularly built towns, roughness lengths are found to be between 0.7 and 1.5 m. and for high-rise urban surfaces (building heights $\geq$20 m), which is the case for part of São Paulo, Grimmond and Oke (1999b) suggested roughness lengths $\geq$2 m. However, we use the morphometric relations of Kastner-Klein and Rotach (2003) to estimate the roughness length and the zero-plane displacement (see Table 3).

The São Paulo urban area is 2700 km^2 (Flores et al. 2016b) when taking into consideration its recent urbanization growth (IBGE 2008). Tarifa and Azevedo (2001) divided the greater São Paulo region into two different land-use classes to obtain a more realistic UHI effect (Table 4): (1) urban type I mostly high-rise buildings (400 km^2); (2) urban type II residential and industrial areas (2300 km^2). These two areas are defined based on satellite imagery and classified according to the original land-cover categories provided by the International Geosphere–Biosphere Programme. The average values for these two urban areas are calculated for the parameters displayed in Table 4.

The input parameters used in the tTEB scheme related to buildings, road materials and the average geometry of the urban area are given in the Online supplementary material. These parameters were obtained from Masson (2000) and Oke (1987), which provide several values for construction materials. Other parameters used in the tTEB scheme, such as the building height, the canyon and building aspect ratios, are related to the geometry of urban areas and

the heat fluxes released by traffic and industrial sources, and are estimated as averaged values proportional to the urban areas of São Paulo (Table 4). We note that, as these average values are associated with a high degree of approximation, more accurate morphological datasets for urban modelling are required.

Lei et al. (2008) concluded that the urban landscape by itself did not enhance precipitation over Mumbai, India, on 26 July 2005. Instead, the SST updated with data from the Tropical Rainfall Measuring Mission and urban effects prescribed by their urban model, created realistic air-temperature gradients that contribute to sustaining a convergence zone over Mumbai.

The default SST data used in ARPS (Global Forecast System model with 1° resolution), are replaced with daily SST data from the Tropical Rainfall Measuring Mission (0.25° resolution), which, when compared with the Global Forecast System data, show a lower SST (close to 1 °C) and larger horizontal gradients of SST around the coast of the state of São Paulo. These differences in SST create realistic air-temperature gradients that help maintain the convergence zone over São Paulo.

4 Synoptic Analysis of 22 August 2014

The wind vectors and pressure reduced to sea level of the Global Forecast System over South America for 22 August 2014 at 1800 UTC are shown in Fig. 3a. The relatively high surface

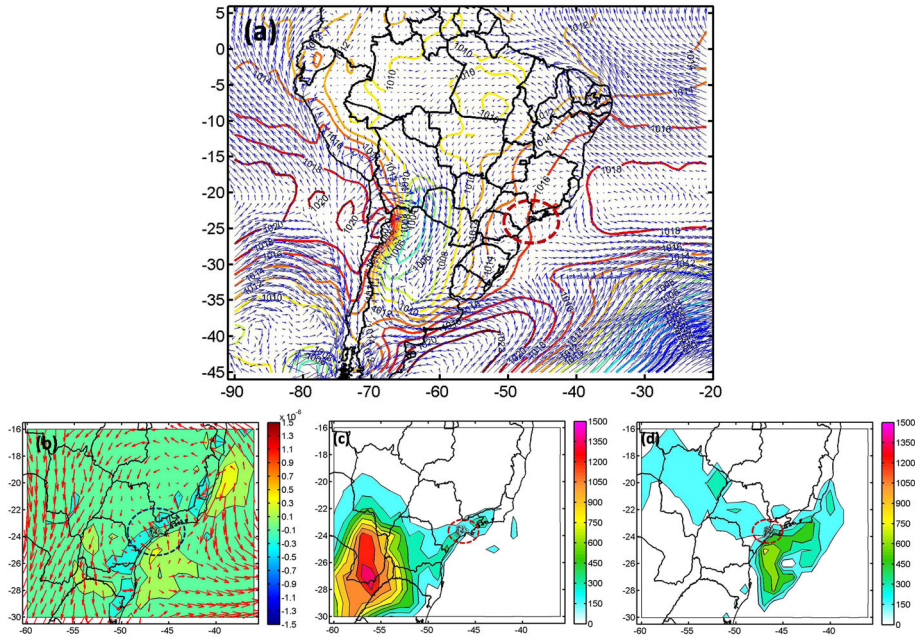

Fig. 3 **a** Reduced pressure to mean sea level (hPa) and horizontal vectors (wind speed in m s^{-1}). *Cold colours* indicate lower values, and warm colours higher values. **b** Moisture divergence flux (g kg^{-1} s^{-1}) at the level of 1000 hPa. **c** Spatial distribution of convective available potential energy (J kg^{-1}). **d** Spatial distribution of convective inhibition (J kg^{-1}). The data are obtained from the Global Forecast System model for 22 August 2014 at 1800 UTC. Longitudes, latitudes and geopolitical contours are indicated. The *dashed circles* indicate the region around São Paulo

pressure over the Atlantic Ocean (23°S, 30°W) induced a north-west/north-east flow over São Paulo during the day. The high pressure region (1016 hPa) oriented south-west to north-east increased instability and clear-sky conditions during the day over São Paulo.

Figure 3b shows the wind speed and moisture divergence flux fields over south-eastern Brazil at 1800 UTC on 22 August 2014. The wind-speed field near São Paulo indicates a sea-breeze circulation and a weak moisture convergence (-0.3×10^{-6} g kg^{-1} s^{-1}). The convective available potential energy is the energy a parcel acquires by lifting and the convective inhibition is the energy inhibiting an air parcel lifting from the surface to the level of free convection. Both fields obtained from the Global Forecast System at 1800 UTC are shown in Fig. 3c and d, respectively. Over São Paulo, the convective available potential energy and the convective inhibition are close to 200 J kg^{-1}, implying deep convection was unlikely.

Figure 4a shows the mean vertical cross-section of mass divergence between 47.5°S and 45.5°S, as a function of latitude and atmospheric pressure obtained from the National Center for Atmospheric Research reanalysis data (at 0.5° resolution) for 22 August 2014 at 1800 UTC. A high divergence zone associated with sea-breeze circulations is observed over the ocean with values close to 1.2 s^{-1} and a weak convergence zone over São Paulo (marked with black triangles), with values close to -0.3 s^{-1} in agreement with the Global Forecast System data (Fig. 3b).

The convergence at 800 hPa and the surface divergence are observed over the ocean, and Fig. 4a shows the mean vertical cross-section of the zonal wind between 47.5°S and 45.5°S as a function of latitude and atmospheric pressure, also obtained from the 0.5° reanalysis data. A low-level jet of 10 m s^{-1} is associated with the convergence between 850 and 800 hPa. Figure 4c, d shows the reanalysis data for the 1000-hPa wind field and the same field for the ARPS 9-km grid simulation, respectively, at 1800 UTC on 22 August 2014, with both showing the sea breeze across São Paulo. Figure 4e shows the wind rose for a weather station (23°29′00″S, 46°30′03″W) for 22 August 2014 with the wind direction veering from the north-east and shifting, with increasing wind speed (to 8 m s^{-1}), to the south-east during the passage of the sea-breeze front. Hence, ARPS simulated these features reasonably well.

5 Analysis of the Results

5.1 Sounding and Surface Measurements

Surface measurements of temperature, relative humidity and wind speed from two automatic weather stations are used to verify simulations, namely the EACH station (station 1) (23°29′00″S, 46°30′03″W), located in the north-eastern region of São Paulo close to the boundary with a rural area (labelled 1 in Fig. 7) and the CINTEC station (station 2) (23°39′05″S, 46°37′21″W) located in the south-western region of São Paulo close to the centre of the urban area (labelled 2 in Fig. 7). Important instrumental characteristics at both stations are shown in the Online supplementary material (Funari and Pereira Filho 2014).

The time series of surface (10 m) air temperature, relative humidity and wind speed for the tTEB and control simulations are obtained from the grid point closest to each station. The diurnal cycle of air temperature obtained at station 2 (Fig. 5a) is better simulated by the tTEB experiment with a maximum of 28 °C and minimum of 12 °C, while the control run underestimates temperatures by 2–4 °C. The correlation coefficients (R^2) for the tTEB and control simulations are 0.92 and 0.81, respectively.

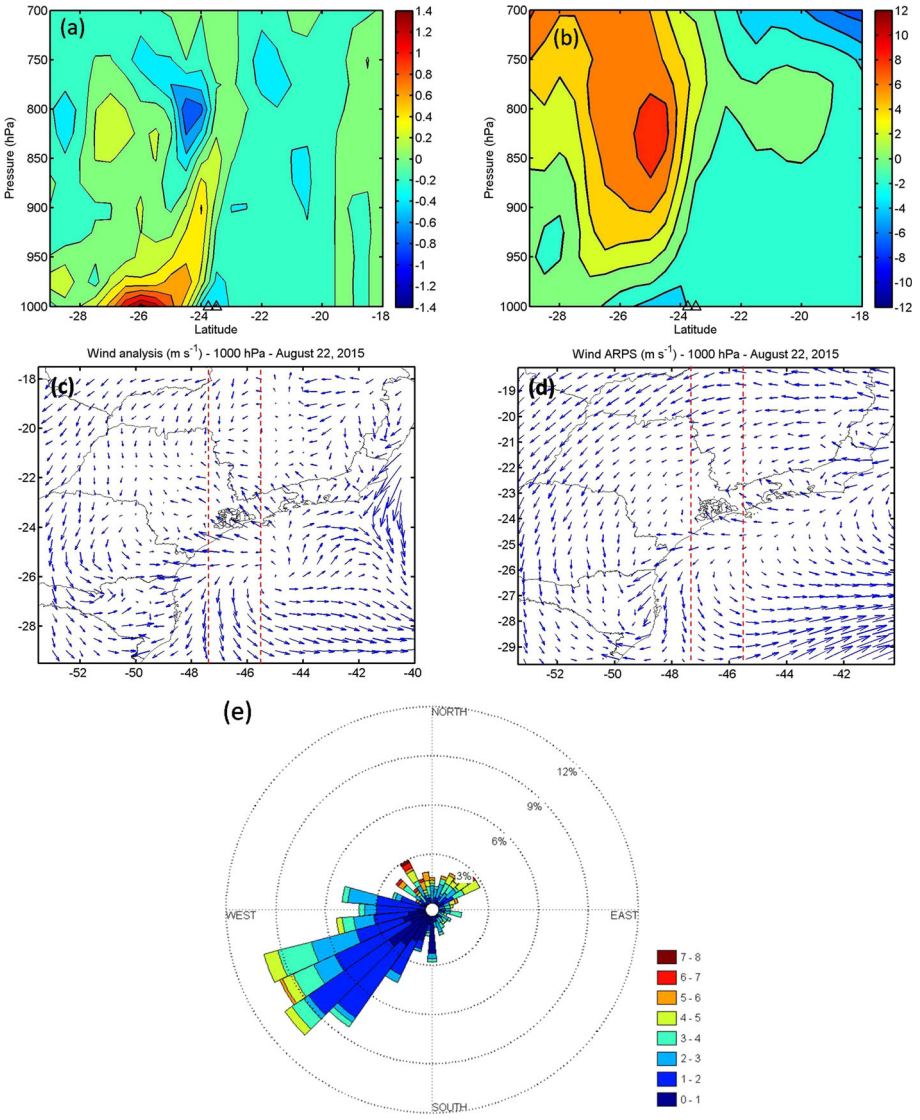

Fig. 4 Mean vertical cross-section of **a** mass divergence (s^{-1}), and **b** zonal wind speeds (m s^{-1}). The fields are averaged between 47.5°S and 45.5°S (marked with *red lines* in **c** and **d**). *Black triangles* at the *bottom* indicate the location of São Paulo. The data are obtained from the Global Forecast System model for 22 August 2014 at 1800 UTC. Comparison of **c** NCEP reanalysis data (resolution 0.5°) and **d** the simulated results of flow circulation at 1000 hPa for the grid of 9 km at 1800 UTC. Longitudes, latitudes and geopolitical contours are indicated. **e** Wind rose for 22 August 2014 at the EACH weather station

Similar results are obtained for the relative humidity (Fig. 5c), with the maximum and minimum relative humidity at 85 and 25%, respectively, for the tTEB experiment. In contrast, the control experiment underestimates the relative humidity by 10–15% at night. The correlation coefficients (R^2) are 0.88 and 0.72 for the tTEB and control experiments, respectively.

The diurnal cycle of wind speed (Fig. 5e) indicates two patterns: (1) low wind speeds between 0.5 and 2 m s^{-1} and, (2) higher wind speeds between 3 and 6 m s^{-1} associated with

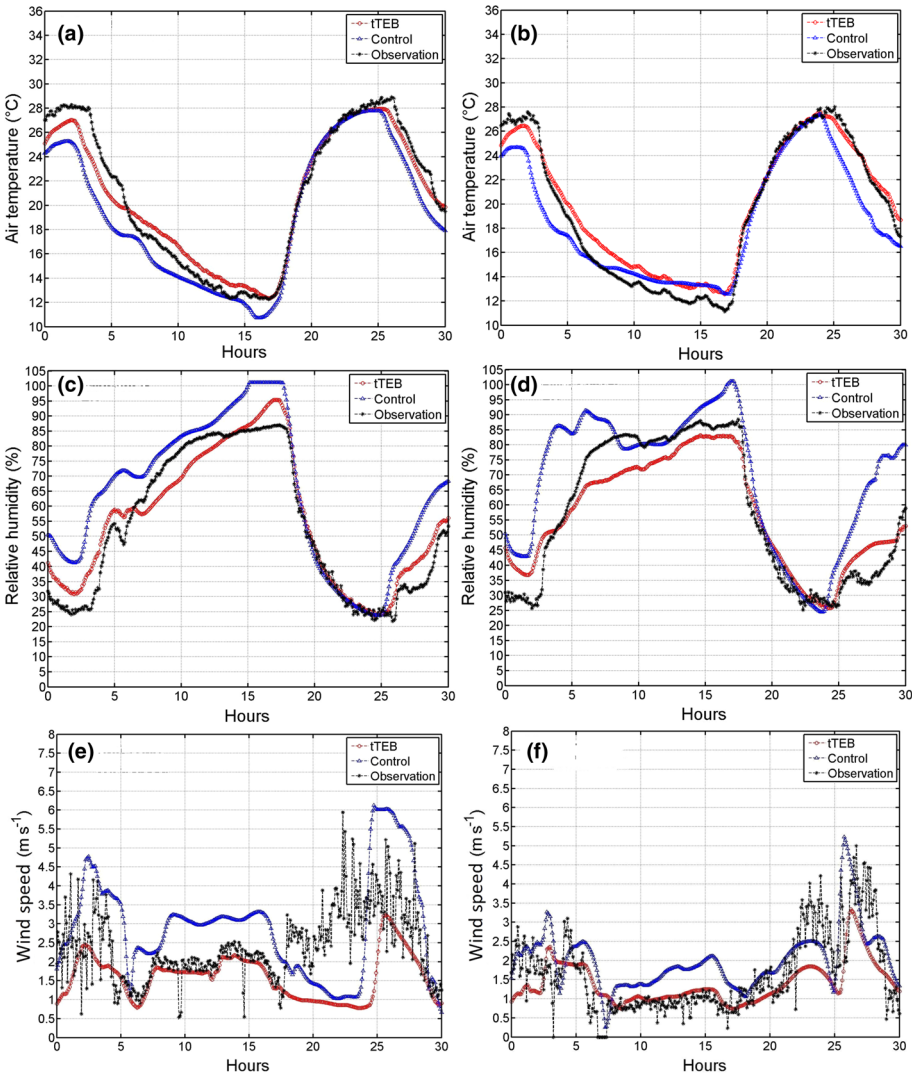

Fig. 5 Comparison of the observed with the simulated air temperature (°C), relative humidity (%) and wind speed (m s^{-1}) from the (**a**, **c**, **e**) EACH and (**b**, **d**, **f**) CINTEC weather stations, respectively. *Black dashed lines* indicate observed data. *Red dashed lines* indicate results with the tTEB scheme and *blue dashed lines* indicate the results of the control experiment. Simulations are performed for the period 1800 UTC on 21 August 2014 to 2400 UTC on 22 August 2014 (30 h)

the sea breeze. The first pattern is better represented by the tTEB experiment, while the second is better represented by the control experiment. While this may be related to drag effects of the urban canopy, which are homogeneous for the tTEB experiment (Table 4), the tTEB experiment did yield a higher correlation coefficient ($R^2 = 0.46$) than the control experiment ($R^2 = 0.38$).

The diurnal cycle of air temperature at station 1 (Fig. 5b) is better represented by the tTEB experiment, with a maximum near 28 °C and minimum under 12 °C. Both experiments overestimate the air temperature by 2 °C in the afternoon and at night since station 1 borders

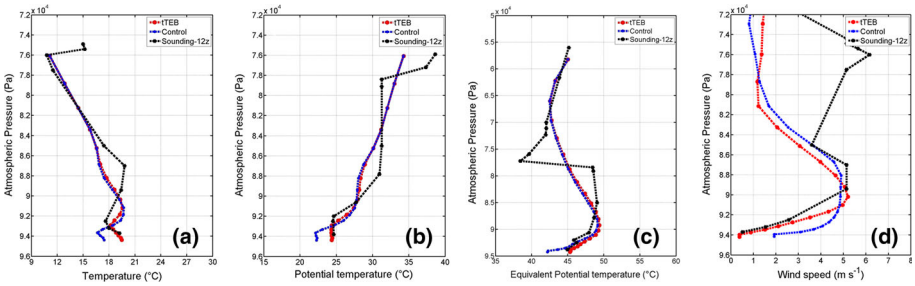

Fig. 6 Comparison between the observed and simulated sounding results for the tTEB and control experiments at the Campo de Marte weather station (23.53°S, 46.63°W) at 1200 UTC on 22 August 2014 for **a** temperature, **b** potential temperature, **c** equivalent potential temperature, and **d** wind speed. *Black dashed lines* indicate observed data. *Red dashed lines* indicate the tTEB experiment and *blue dashed lines* indicate the control experiment

the rural and urban areas. The correlation coefficients are 0.92 and 0.85 for the tTEB and control experiments, respectively.

The diurnal cycle of relative humidity compares better with the tTEB simulation (Fig. 5d) with a maximum of 85% and a minimum of 25%, and the control experiment underestimates the relative humidity by about 15–20% in the afternoon and night. The correlation coefficients are 0.90 and 0.81 for the tTEB and control simulations, respectively.

The diurnal cycle of wind speed (Fig. 5f) indicates lower and higher wind-speed ranges, with the first between 0.5 and 1 m s^{-1} and the second between 1.5 and 5 m s^{-1}. The latter wind-speed range is associated with the sea breeze. Similarly for station 2, the lower range of wind speed is better simulated with the tTEB experiment, while the higher range with the control experiment. The correlation coefficients are 0.52 and 0.46 for the tTEB and control simulations, respectively.

The sounding profiles provided by the University of Wyoming are useful for quantifying the vertical structure of the atmosphere. Figure 6a compares the observed sounding data with the results of the tTEB and control experiments for the air temperature at the Campo de Marte (23.52°S, 46.63°S) station at 1200 UTC. For the first atmospheric levels (around 940 hPa), the results of the tTEB experiment match better with observations than the results of the control experiment, with temperature differences close to 2 °C.

Similar results are obtained for the potential temperature (Fig. 6b), which indicates a well-defined shallow mixed layer up to 920 hPa. The results of the tTEB experiment are generally closer to observations, with the control results being about 2 °C lower. Results for the equivalent potential temperature show a stable boundary layer up to 900 hPa, with the tTEB results better matching observations. For the wind speed, the sounding data indicate a low-level jet with maximum values close to 5 m s^{-1} at 880 hPa. This structure is well simulated by both the tTEB and control experiments, and above 860 hPa, the maximum wind speeds are underestimated in both experiments.

5.2 Land-Surface Temperature from the Moderate Resolution Imaging Spectroradiometer

The MODIS instruments on board the Terra and Aqua satellites provide measurements of surface variables at 36 wavelength bands, including near infrared and visible spectra. TERRA satellite has a near polar sun-synchronous orbit, which passes in view of any point on Earth

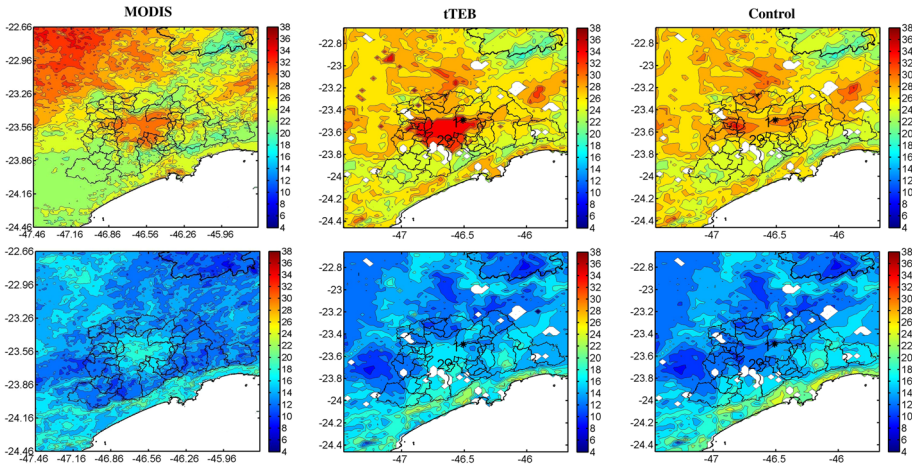

Fig. 7 (*first row*) Spatial distribution of the LST (°C) at 1930 UTC (day) of 22 August 2014 from MODIS data for an eight-day period (*left*), and the tTEB (*centre*) and control (*right*) experiments. (*second row*) Spatial distribution of LST (°C) at 0600 UTC (night) on 22 August 2014 from MODIS data of an eight-day period (*left*), and the tTEB (*centre*) and control (*right*) experiments

twice daily at 1030 LT and 2230 LT. The MODIS thermal infrared sensors measure the top-of-the-atmosphere radiances, from which brightness temperatures are derived. These brightness temperatures differ from the actual LST by 1–5 K, due to the non-vertical satellite viewing angle, the urban geometry, the sub-pixel variation of the surface temperature, the variable surface emissivity and several atmospheric effects (Dousset and Gourmelon 2003).

These effects are removed in estimations of the LST from space using a day-night method designed to take advantage of the unique capability of the MODIS sensor (Wan 1999). This method uses day-night pairs of thermal infrared data in seven MODIS bands to simultaneously retrieve the LST and band-averaged emissivities without knowing the water vapour and atmospheric-temperature profiles to a high degree of accuracy (Wan and Li 1997). Furthermore, to generate more regionally-representative urban-temperature estimates, the three-dimensional roughness of urban surfaces were considered, which is scale dependent in the satellite images (Voogt and Grimmond 2000).

The MOD11 product contains level-2 and level-3 LST and emissivity retrieved from MODIS data at spatial resolutions of 1 and 5 km over global land surfaces under clear-sky conditions. We use the level-3 MODIS global LST data (MOD11A2), which are composed of a daily 1-km LST product (MOD11A1), and stored on a 1-km sinusoidal grid as the average value of the clear-sky LST during an eight-day period. Figure 7 shows the spatial pattern of LST obtained from the MODIS sensor in comparison with the tTEB and control experiments around São Paulo at 1930 UTC (day) and 0600 UTC (night).

At 1930 UTC (day), the LST is overestimated by the tTEB experiment due to the use of the same averaged urban parameters (Table 4) for the entire urban canopy, which is unrealistic due to the marked heterogeneity of the urban surface. However, the spatial pattern of the LST is better represented in the tTEB experiment in comparison with the control experiment. The two-dimensional correlation coefficient at 1930 UTC (day) for the tTEB experiment (control experiment) is 0.84 (0.81), and at 0600 UTC (night), the two-dimensional correlation coefficient for the tTEB experiment (control experiment) is 0.74 (0.68).

5.3 Impact of Topography

Air motion induced by topographic features depends on the morphology, such as height, length, width and spacing between successive ridges, as well as on the properties of the airflow itself, such as the wind direction relative to the barrier, and the vertical profiles of wind speed and stability (Barry 2008). The general classes of flow for an ideal fluid encountering an obstacle, are described with reference to the Froude number Fr, which is the ratio of internal viscous forces to gravitational forces (Barry 2008),

$$Fr = 2\,\pi\, U\, /\, h\, S^{1/2}, \tag{3}$$

where U is the undisturbed flow speed, h is the mountain height and S is the static stability. The Froude number can also be interpreted as the ratio of kinetic energy of the air encountering a barrier to the potential energy necessary to surmount the barrier. For stratified flows, Fr tends to zero, and the flow tends to go around the obstacle.

The atmosphere over São Paulo was highly stable during the morning on 22 August 2014 with north-westerly flow associated with the land breeze channelled by the hills around São Paulo (Fig. 2c). Figure 8 (first row) shows the surface wind vectors and wind speeds at 0900 UTC (early morning) for both the tTEB and control experiments. The circle indicates the centre of the urban canopy where wind speeds are reduced by 2.5 m s^{-1} in comparison with the semi-desert canopy, due to the higher frictional drag of the canyon walls. Moreover, the circulation of the mountain-valley inversion increases the wind speeds at the edge of the hills up to values close to 5 m s^{-1}.

In general, local flow perturbations over hills are related to two basic processes that modify the pressure gradient on a local scale. Taylor (1977) shows that, for two-dimensional flows in a neutral atmosphere (ignoring the shear stress and Coriollis effects), the dynamic pressure gradient P_D on the upwind side of the hill and the hydrostatic pressure gradient induced by heating P_H are related by,

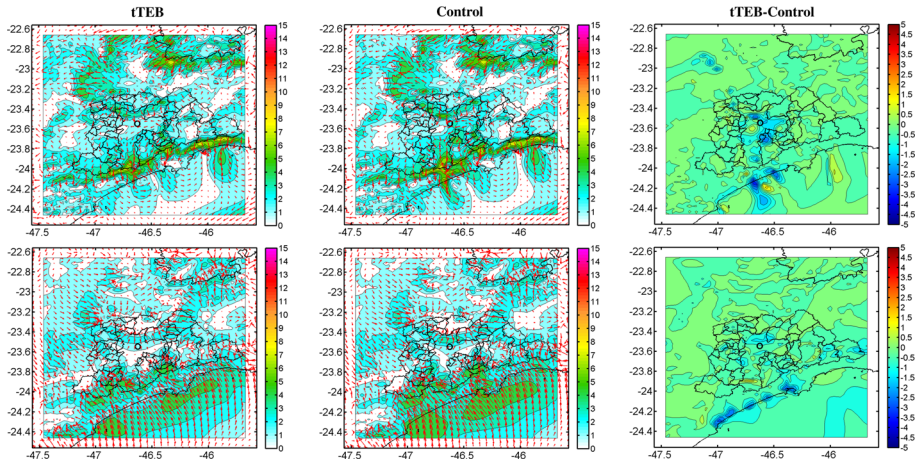

Fig. 8 (*first row*) Surface wind vectors and wind speed (m s^{-1}) over São Paulo for 22 August 2014 at 0900 UTC (night) for the tTEB and control experiments, and their difference. (*second row*) Surface wind vectors (m s^{-1}) and wind speed over São Paulo for 22 August 2014 at 1600 UTC (day) for the tTEB and control experiments, and their difference. The *black circle* indicates the centre of the urban area of São Paulo

$$P_D = -\rho\, U^2\, h\, /\, L^2, \tag{4a}$$

$$P_H = -\rho\, g\, \Delta\theta\, h^*\, \theta\, L \tag{4b}$$

where L is the width of the hill, h is the height of the hill, ρ is the air density, U is the upwind flow speed, θ is the upwind potential temperature, $\Delta\theta$ is the increase of potential temperature over the hill, h^* is the smaller of h and h_s, which is the height of the superadiabatic layer near the surface, and g is the acceleration due to gravity. By a dimensional analysis of the ratio of P_D/P_H for the selected values of L, h and h^*, Taylor (1977) showed that for steeper slopes of 1:10, the dynamic and thermal effects have similar magnitudes, while for large-scale hills ($L \sim 10\,\text{km}$, $h = h^* = 100\,\text{m}$), thermal effects dominate.

The topographic barrier of the Serra do Mar mountain range separating São Paulo from the ocean (Fig. 2c) is a large-scale hill with $L \approx 200\,\text{km}$ and $h \approx 800\,\text{m}$, which extends along the coast with its normal vector oriented in the south-east direction. Provided there is sufficient daytime heating, at approximately 1300 UTC, the sea breeze ascends the slope of the Serra do Mar, develops into a well-defined mountain-plain circulation, and forms a lee-side convergence zone, which propagates inland.

Due to the horizontal extension of the Serra do Mar mountain range, the thermal pressure-gradient effects dominate over the dynamic effects. Figure 8 (second row) shows the surface wind vectors around São Paulo at 1600 UTC for the tTEB and control experiments, where it is observed that the sea breeze flows inland along the coast of São Paulo. In the tTEB experiment, the horizontal wind speed is reduced by up to $3\,\text{m s}^{-1}$ over urban areas along the coast due to the higher surface roughness.

Figure 9 (first row) shows the cross-section of the vertical wind speed for the tTEB and control experiments at 1500 UTC, where a well-defined positive value at the boundary of the Serra do Mar mountain range (≈23.95°S) is observed up to 2000 m above sea level, with maximum values close to $0.25\,\text{m s}^{-1}$ at 500 m. The vertical wind speeds of both experiments are similar, but higher in the tTEB experiment due to the effects of the urban canopy along the coast, which changes the thermal and dynamic conditions of this area (Fig. 2a).

The vertical cross-section of the mean moisture divergence flux for the TEB and control experiments is shown in Fig. 9 (second row). The pattern of convergence divergence associated with the mountain-plain circulation, extends from the Serra do Mar to the urban area of São Paulo. The strong convergence zone above the Serra do Mar, which is associated with the sea breeze and differential heating, reaches values close to $-7\,\text{g kg}^{-1}\,\text{s}^{-1}$ up to 600 m above sea level, while the divergence zone over the centre of São Paulo reaches values close to $2\,\text{g kg}^{-1}\ \text{s}^{-1}$.

The heating and dynamic pressure gradients on the upwind side (Eq. 4) of the Serra do Mar mountain range generate a flow acceleration zone in the tTEB and control experiments, as can be observed in Fig. 9 (third row), which shows the surface acceleration vectors and acceleration at 1600 UTC. The maximum acceleration magnitudes reach values close to $2.4 \times 10^{-3}\,\text{m s}^{-2}$. For the tTEB experiment, the surface acceleration vectors are channelled by the topography (Fig. 2c) and directed towards the urban area of São Paulo, and are slightly advanced in relation to the acceleration vectors for the control experiment (see the third row of Fig. 9).

The patterns of the vertical wind speed and moisture divergence flux (Fig. 9) reveal the faster propagation of the sea breeze when passing through the Serra do Mar mountain ranges according to the tTEB experiment, which is caused by the greater horizontal pressure gradient that exists between this region and the coast, as a consequence of the dynamic and thermal effects generated by the urban canopy.

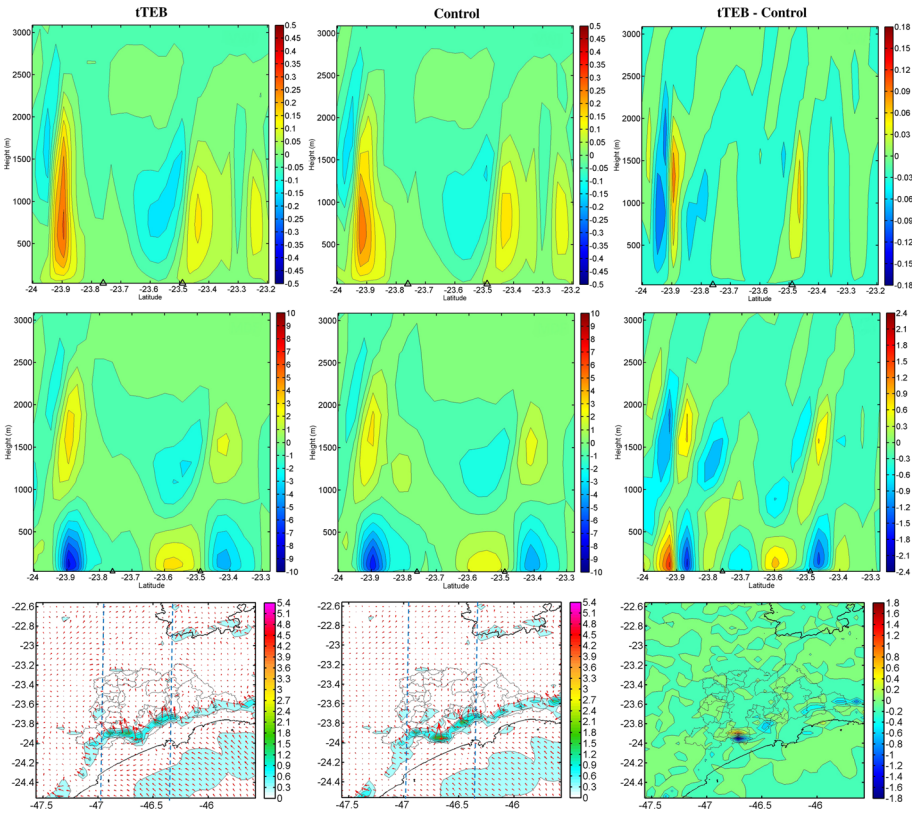

Fig. 9 (*first row*) Vertical cross-section of the mean vertical wind speed (m s^{-1}). (*second row*) Vertical cross-section of mean moisture divergence flux (g kg^{-1} s^{-1}). (*third row*) Surface acceleration vectors and acceleration (m s^{-2}) around São Paulo. The mean values are averaged from 46.9°W to 46.42°W (showed as *blue lines*) at 1500 UTC for the tTEB (*first column*) and control (*second column*) experiments, and their difference (*third column*)

5.4 Impact of Coupling ARPS with tTEB

The simulation results discussed above indicate that the non-hydrostatic mesoscale model, when coupled with the explicit urban energy budget scheme demonstrates an enhanced ability, in comparison with the default option. Improvements are observed in time series of the surface temperature, relative humidity and wind speed as measured at two automatic weather stations, and the observed vertical profiles of temperature, equivalent potential temperature and wind speed over São Paulo for the typical sea-breeze event of 22 August 2014. Here, we discuss the effects of the coupled system.

5.4.1 Temperature and Energy Fluxes (Simulation of the Effect of UHI)

A valid simulation of the surface air temperature is important because the heat flux from the surface influences the lower boundary-layer stability. The UHI effect appears to be well simulated by the coupled system around São Paulo, for both day and night. Figure 10 shows

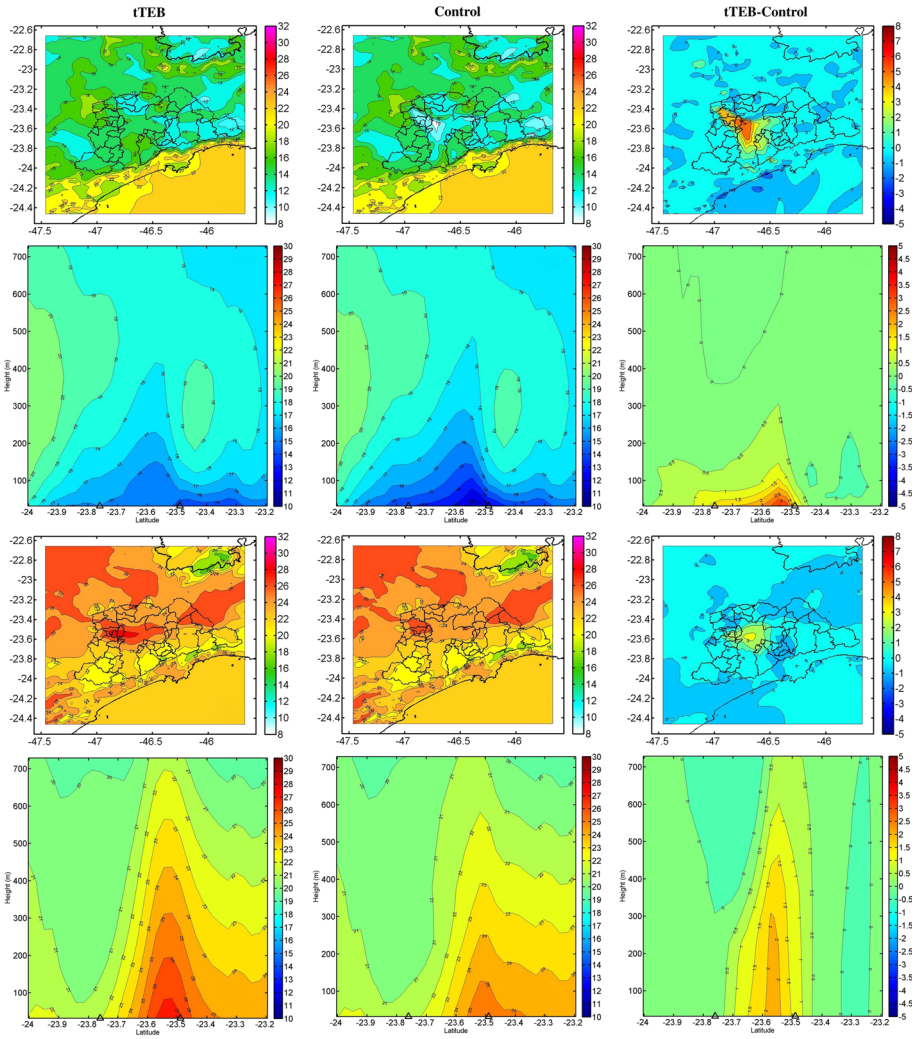

Fig. 10 Horizontal spatial distribution of the 10-m surface air temperature (°C) at 0900 UTC (*first row*) and 2000 UTC (*third row*) on 22 August 2014. Vertical cross-section of air temperature (°C) from 46.9°W to 46.42°W at 0900 UTC (*second row*) and 2000 UTC (*fourth row*) on 22 August 2014 for the tTEB (*first column*) and control (*second column*) experiments, and their difference (*third column*)

the surface air temperatures at 0900 UTC (early morning) and 2000 UTC (late afternoon) for the tTEB and control experiments, and their difference.

At 0900 UTC (Fig. 10, first row), the land breeze is channelled by the hills around São Paulo (Fig. 8). At this time, the air-temperature difference between both experiments reaches close to 6 °C. At 2000 UTC (Fig. 10, third row), the sea breeze passes over the centre of São Paulo. At this time, the air-temperature difference between the experiments reaches close to 3 °C. Throughout the day, the warming zone extends from the city centre to the north-west, with 1–3 °C higher temperatures than the surroundings. During the night, the warming zone extends from the city centre to the south-west with 1–6 °C higher temperatures than the surroundings.

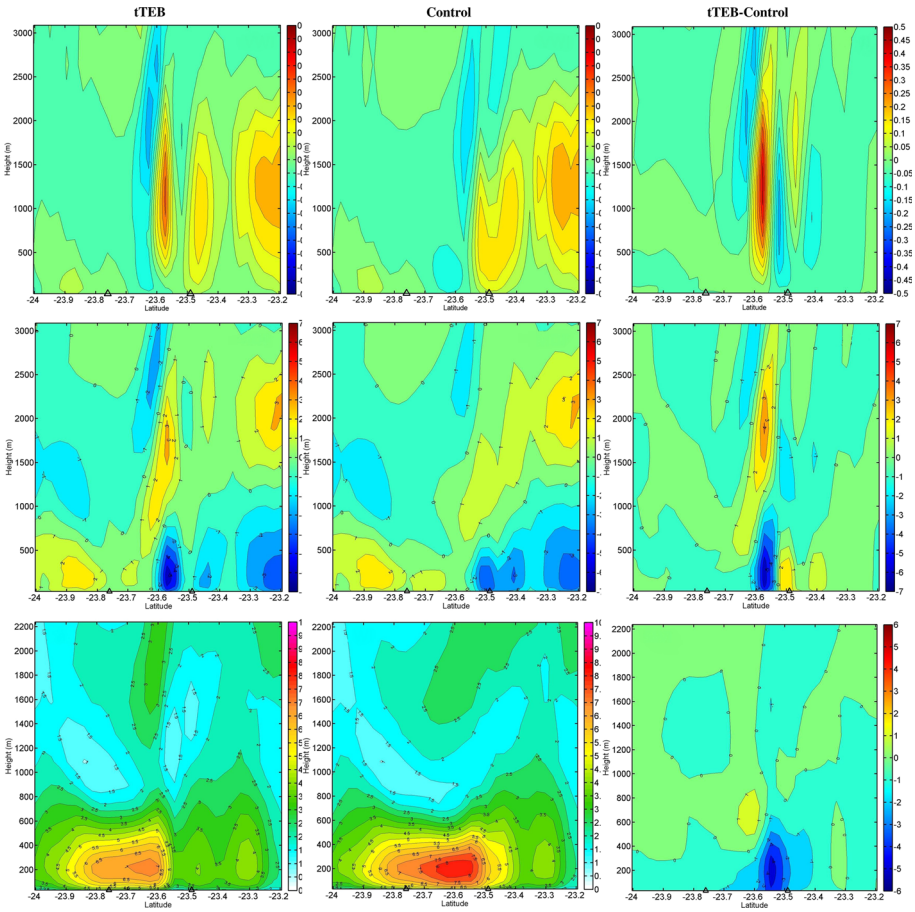

Fig. 11 (*first row*) Vertical cross-section of the mean vertical wind speed (m s^{-1}). (*second row*) Vertical cross-section of mean moisture divergence flux (g kg^{-1} s^{-1}). (*third row*) Vertical cross-section of wind speed (m s^{-1}). The mean values are obtained from 46.9°W to 46.42°W (Fig. 9) at 2000 UTC on 22 August 2014 for the tTEB (*left*) and control (*centre*) experiments and their difference (*right*). *Black triangles* indicate the limits of the urban canopy

The UHI effect is apparent for most of the day, and is more significant downwind of the city. Figure 10 (second row) shows the vertical cross-section of air temperature at 0900 UTC for the tTEB and control experiments and their difference. The higher air temperatures are found at the surface with values close to 4 °C, with the warming effects decreasing by up to 0.5 °C at 300 m above the surface. In contrast, at 2000 UTC (Fig. 10 fourth row), the higher air temperatures are typically found up to 700 m above the surface, and extend to the north-west direction, with warming effects from 0.5 °C up to 2 °C.

To investigate the effects of heating of the urban surface on the evolution of the UHI intensity, we analyze the surface energy budget in the urban area. The energy components are averaged over the entire urban area for the entire diurnal cycle. The surface energy budget is

$$Q^* + Q_F = Q_H + Q_E + \Delta Q_S, \tag{5}$$

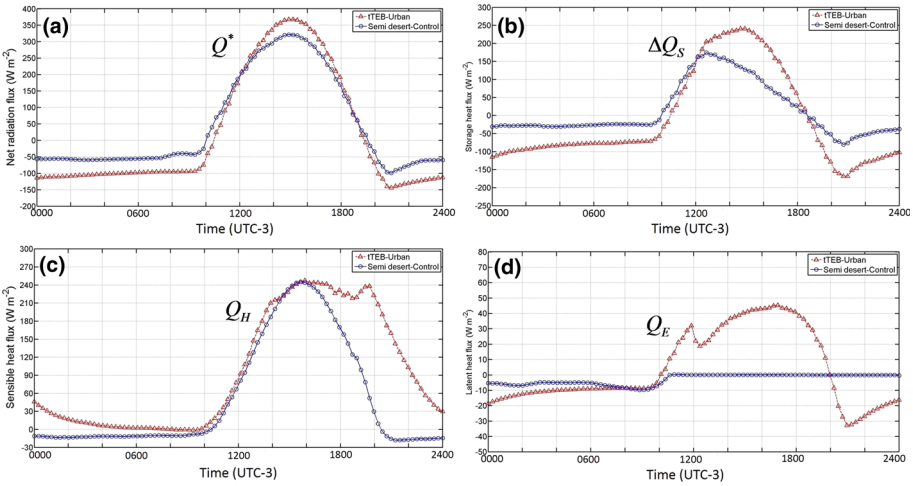

Fig. 12 **a** Diurnal cycle of mean net radiation flux absorbed by the surface. **b** Diurnal cycle of mean storage heat flux. **c** Diurnal cycle of mean sensible heat flux. **d** Diurnal cycle of mean latent heat flux. The mean values are calculated over the entire urban and semi-desert canopy for 22 August 2014

where Q^* is the net all-wave irradiance, Q_F is the anthropogenic heat flux, Q_H is the surface sensible heat flux and Q_E is the surface latent heat flux. The storage heat flux ΔQ_S represents the total heat transfer to/from the urban surface/ground, which includes buildings (roofs and walls) and roads, and is equivalent to the ground heat flux. The net all wave irradiance Q^* is composed of the net shortwave Q_K and longwave irradiances Q_L,

$$Q^* = Q_K + Q_L = (K_\downarrow - K_\uparrow) + (L_\downarrow - L_\uparrow), \tag{6}$$

where $K_\downarrow$ and $L_\downarrow$ are the incoming short wave and longwave irradiances, and $K_\uparrow$ and $L_\uparrow$ are the outgoing shortwave and longwave irradiances, respectively. Figure 12a shows the diurnal cycle of the mean net radiation flux absorbed by surface for the tTEB and control experiments.

During the day, the differences of the net irradiance between the semi-desert and urban canopy reach values close to 45 W m^{-2} due to the reduced albedo of the urban canopy, and consequently the decrease of shortwave irradiance ($K_\uparrow$). At night, the increase of outgoing longwave radiation ($L_\uparrow$) is observed, because the urban area is warmer than the semi-desert canopy, and consequently, the net radiation flux is more negative. In this case, the differences of net irradiance between semi-desert and urban canopy reach values close to -40 W m^{-2} (Oke 1987).

The urban-source terms at night are very different to those during the daytime. A nocturnal excess in heat storage, which accumulates during the day, is balanced by an increase of net outgoing longwave irradiance and sensible heat flux. The impact on the 10-m temperature is increased further during the night (Fig. 5), even though the differences between the sensible heat flux are smaller than during the day (Fig. 12c). This fact may be explained by the stable stratification during the night, which retains the urban-source terms much closer to the ground than for the unstable stratification during the day (Bohnenstengel et al. 2011).

For the control experiment, the semi-desert canopy exhibits a thermally-extreme climate, with higher temperatures at day and lower temperatures at night, as a result of the lack of moisture, and the concentration of heat in the uppermost sand layer. In contrast, for the

tTEB simulation, the turbulent sensible heat flux within the urban canopy is the primary factor removing the daytime surplus of net radiation. However, in contrast to a semi-desert canopy, the evapotranspiration in the urban canopy, which is generated by traffic and industrial sources (Table 4), is the next largest heat loss for the system, indicating that water is still readily available, despite the waterproofing effects of urban development.

As illustrated in Fig. 12c,d, which shows the time series of turbulent sensible and latent heat fluxes over urban and semi-desert canopies, the turbulent sensible heat flux has a significant phase lag, with maximum values close to 240 W m^{-2} detected, which remains positive into the late evening (after sunset) in the urban canopy. The continued warming of the atmosphere by turbulent heat transport is important for the growth of the nocturnal heat island typical of urban environments.

For the turbulent latent heat flux, the semi-desert canopy shows a lower diurnal variation resulting from the lack of moisture. In contrast, for the urban canopy, there is a significant transport of latent heat at both day and night, with maximum flux values close to 50 W m^{-2} and a minimum of -30 W m^{-2}. Because of the absence of precipitation during the day, the latent heat flux is largely produced by the moisture generated by the exhaust from traffic and industrial sources inside the urban area (see Online supplementary material).

The spatial distribution of the sensible and latent heat fluxes at 1830 UTC around São Paulo for the tTEB and control experiments are shown in Fig. 13 (first and second rows, respectively). For the sensible heat flux, the higher values are located in the south-east region of the city with values close to 360 W m^{-2}, which is then advected by the sea breeze to the north-west region (Fig. 10). For the latent heat flux, the higher values are located in the centre of the city, with maximum values close to 60 W m^{-2}.

A vertical cross-section of the mean TKE for the tTEB and control experiments at 1915 UTC is shown in Fig. 13 (third row), with the tTEB experiment generating stronger turbulence over São Paulo with TKE values from 1.4 $m^2 s^{-2}$ at 400 m to 0.2 $m^2 s^{-2}$ at 2000 m. The enhanced TKE generates an effective mixing of pollutants inside the urban region.

5.4.2 Flow Convergence

The convergence zone created by the advance of the sea breeze over the Serra do Mar mountain range, propagates inland to the centre of São Paulo. From the simulation results, the sea breeze arrives at the centre of São Paulo between 1830 UTC and 1900 UTC, and a vertical updraft is apparent in both the control and tTEB simulations (not shown).

Figure 11 (first row) shows the vertical cross-section of vertical wind speed at 2000 UTC for both experiments, and their difference. The enhancement in vertical wind speed for the tTEB experiment reaches close to 0.45 m s^{-1} from the surface up to 2400 m above ground. In contrast, for the control experiment, the vertical velocity component reaches values close to 0.15 m s^{-1} up to 1500 m above the surface.

Urbanization increases the flow convergence in the upwind direction due to roughness changes and the thermal conditions inside the urban canopy. Figure 11 (second row) shows the vertical cross-section of the mean moisture divergence flux for the tTEB and control simulations at 2000 UTC. For the tTEB experiment, a significant convergence zone develops over São Paulo from the surface to a height of 1000 m, with maximum values close to -6 g kg^{-1} s^{-1}. A corresponding divergence zone developed above up to 2500 m above the surface, with maximum values close to 3 g kg^{-1} s^{-1}.

In contrast, for the control experiment, the convergence and the vertical wind speed are lower, with values close to -3 g kg^{-1} s^{-1} and 0.15 m s^{-1}, respectively. In addition, the divergence zone at 2500 m above ground is weaker in comparison with the divergence in the tTEB

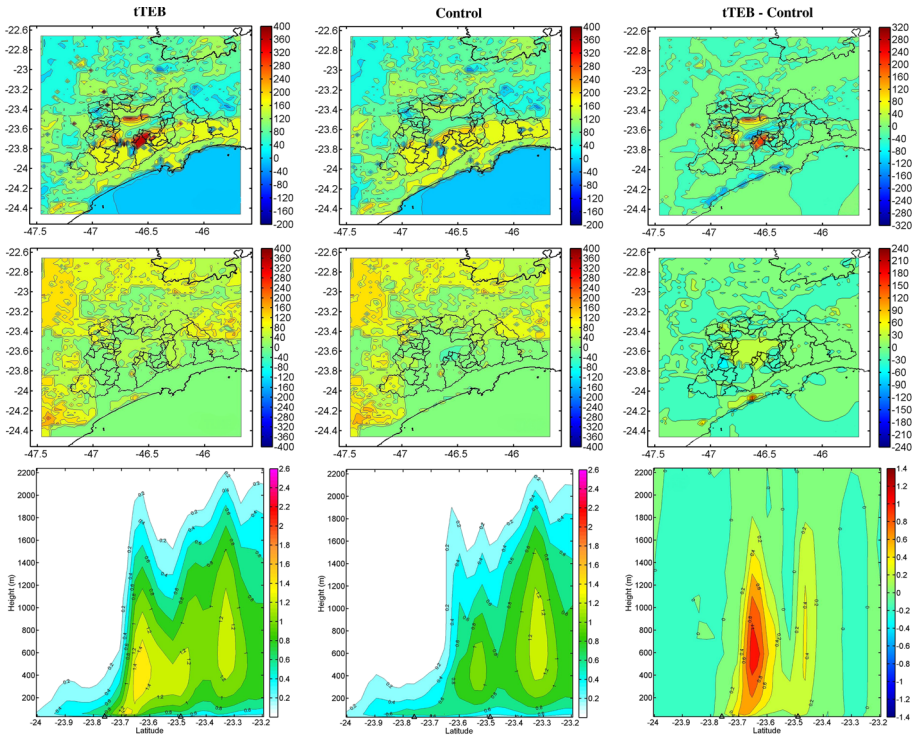

Fig. 13 (*first row*) Spatial distribution of the turbulent sensible heat flux. (*second row*) Spatial distribution of turbulent latent heat flux (TLHF). (*third row*) Vertical cross-section of mean TKE between 46.9°W and 46.42°W (Fig. 9). All variables are obtained at 1830 UTC on 22 August 2014 for the tTEB (*left*) and control (*centre*) experiments, and their difference (*right*). *Black triangles* indicate the limits of the urban canopy

experiment. Moreover, the sea-breeze front slows towards the urban canopy due to changes of roughness and thermal conditions. The low-level offshore wind speeds are lower for the tTEB experiment in comparison with the control experiment.

Figure 11 (third row) shows the vertical cross-section of the wind speed for the tTEB and control experiments at 2000 UTC. The control run produces wind speeds from 8 m s^{-1} to 2.5 m s^{-1} below 650 m, with the sea-breeze front located at ≈23.4°S. In contrast, the tTEB experiment gives wind speeds from 7 m s^{-1} to 2.5 m s^{-1} below 850 m, with the sea-breeze front located at 23.55°S. As a consequence, the sea-breeze front in the tTEB experiment is delayed by a distance of ≈0.15° in comparison with the sea-breeze front in the control experiment. Figure 14 (first row) shows the surface wind vectors and wind speeds over São Paulo at 2000 UTC. For the tTEB experiment, wind speeds are up to 6 m s^{-1} lower over the urban area in comparison with the control experiment, resulting from the urbanization converging flow upwind of São Paulo.

For the tTEB experiment, the UHI circulation prevents the advance of the sea-breeze front, as mentioned above, because of the opposite acceleration of the sea-breeze cell in the centre and northern part of São Paulo (Freitas et al. 2007). In the control experiment, there is no acceleration counteracting the propagation of the sea-breeze front. Figure 14 (second row) shows the acceleration vectors and magnitudes over São Paulo at 2000 UTC for the tTEB and control experiments and their difference.

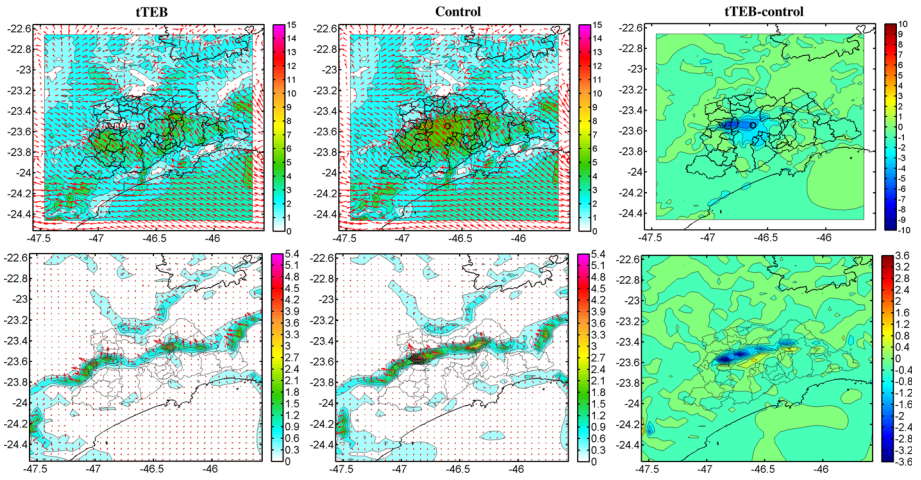

Fig. 14 (*first row*) Surface wind speed over São Paulo for 22 August 2014 at 2000 UTC (day) for the tTEB and control experiments, and their difference. (*second row*) Surface acceleration over São Paulo for 22 August 2014 at 2000 UTC (day) for the tTEB and control experiments, and their difference. The *black circle* indicates the centre of the urban area of São Paulo

The sea-breeze front is decelerated and retarded over the urban canopy of São Paulo up to 3.2×10^{-3} m s^{-2} for the tTEB experiment in comparison with the flow acceleration of the control experiment. After the UHI effects disappear, the sea breeze continues its propagation inland, and is slightly more intense in the control experiment in comparison with the tTEB experiment (not shown).

6 Conclusions

We provide a detailed description of the coupling between the mesoscale atmospheric model ARPS and the tTEB urban energy budget scheme. The coupled system is used to simulate the interaction between the sea-breeze, mountain-valley and UHI circulations for the typical sea-breeze event on 22 August 22 2014 without deep convection over the metropolitan area of São Paulo, Brazil. Experiments are performed with urban-canopy scheme (the tTEB experiment) and with the semi-desert scheme (the control experiment), which is the default type used in ARPS.

For the nighttime and early morning periods, the model generates a well-defined land-breeze circulation, which is channelled by the hills around São Paulo. For the tTEB experiment, the wind speeds are reduced around the urban canopy due to frictional effects of the urban roughness. At 1300 UTC, the sea breeze ascends the slope of the Serra do Mar mountain range, and generates a well-defined moisture convergence zone, with vertical velocity components, that propagates inland. The sea-breeze front is then accelerated due to the dynamic and thermal pressure gradients generated by the Serra do Mar mountain range.

When the sea breeze and the associated convergence system arrive at the centre of the urban area, the thermal and dynamic effects of the UHI increase the moisture convergence and vertical wind speeds at 1800 UTC. This causes the sea breeze to stall over the city for two hours, reducing the flow speed and acceleration, and the transport of a large amount of moisture from the surface to the upper levels of the atmosphere.

The contrasting thermal effects of the UHI effect for day and night show that the dense urbanized regions generate higher air temperatures by up to 3 °C (6 °C) at day (night) compared with the default case with the semi-desert canopy parametrization. The comparison of the spatial pattern of the soil temperature with LST data from MODIS for day and night shows an acceptable level of agreement. The urban area of São Paulo also alters the diurnal phase of terms of the surface energy balance. Over the urban surface, the net radiation flux at the surface increases during the day because of the reduced albedo of the urban canopy in comparison with the semi-desert canopy.

Analysis of the diurnal cycle of the surface energy balance during the day reveals a large increase in the sensible heat flux and the heat storage for the urban canopy compared with the semi-desert canopy, with the sensible heat flux also exhibiting a significant phase lag, which remains positive into the late evening. Hence, the continued warming of the atmosphere by turbulent heat exchange leads to the formation of the nocturnal heat island.

The increased uptake of heat during the day, which is subsequently released at night, is the most important reason for the difference in surface sensible heat at night, which stems from the reduced evapotranspiration in the urban area. For the urban canopy, the diurnal cycle of the latent heat flux exhibits a higher amplitude than the values for the semi-desert canopy. Because of the absence of rainfall during the day, the latent heat flux is mainly produced by anthropogenic sources inside the urban area.

The comparison between the modelled and observed time series of air temperature, relative humidity and wind speed at the surface of São Paulo, and the simulations of the interactions between the sea-breeze, mountain-valley and UHI circulations for both the day and night, suggest that the explicit representation of the urban canopy improves the simulation of the local circulations.

An important limitation of the present study is the poor representation of the urban area with constant values for specific parameters, such as geometric features, albedo and the emissivity of the urban canopy, as well as anthropogenically generated fluxes. As a consequence, additional research using more detailed urban features is necessary. Another limitation is the omission of urban aerosols that affect precipitation processes. The generation of a smaller size distribution of droplets is caused by the increase in aerosol concentrations resulting from anthropogenic sources, which can suppress rainfall above and downwind of urban areas.

Acknowledgements We wish to thank to the "Conselho Nacional de Desenvolvimento Cientifico e Tecnologico" (CNPQ) (302349/20146) for the financial support during the research period. We also thank Dr. Ming Xue for important suggestions that helped improve the present manuscript.

References

Amorim J, Rodrigues V, Tavares R, Valente J, Borrego C (2013) CFD modelling of the aerodynamic effect of trees on urban air pollution dispersion. Sci Total Environ 461–462:541–551

Arnfield A, Mills G (1994) An analysis of the circulation characteristics and energy budget of a dry, asymmetric, eastwest urban canyon. II. Energy budget. Int J Climatol 14:239–261

Barry RG (2008) Mountain weather and climate, 3rd edn. Cambridge University Press, Cambridge

Bohnnenstengel S, Evans S, Clark P, Belcher S (2011) Simulations of the london urban heat island. Q J R Meteorol Soc 137:1625–1640

Businger J, Wyngaard JC, Izumi Y, Bradley EF (1971) Flux-profile relationships in the atmospheric surface layer. J Atmos Sci 28:181–189

Byun D (1990) On the analytical solutions of flux-profile relationships for the atmospheric surface layer. J Appl Meteorol 29:652–657

Chen F, Pielke R, Mitchell K (2001) Development and application of land surface models for mesoscale atmospheric models: problems and promises. Am Geophys Union 1:107–136
Cotton W, Pielke R Sr, Walko R, Liston G, Tremback C, Jiang H, Mcanelly R, Harrington J, Nicholls M, Carrio G, Mcfadden J (2003) Rams 2001: current status and future directions. Meteorol Atmos Phys 82:5–39
Deardorff J (1972b) Parameterization of the planetary boundary layer for use in general circulation models. Mon Weather Rev 100:93–106
Dousset B, Gourmelon F (2003) Satellite multi-sensor data analysis of urban surface temperatures and land cover. J Photogramm Remote Sens 58:43–54
Dudhia J, Bresch JF (2002) A Global Version of the PSU-NCAR Mesoscale Model. Mon Wea Rev 130:2989–3007
Flores J, Karam H, Marques Filho E, Pereira Filho A (2016a) Estimation of atmospheric turbidity and surface radiative parameters using broadband clear sky solar irradiance models in rio de janeiro-brasil. Theor Appl Climatol 123:593–617
Flores J, Pereira Filho A, Karam H (2016b) Estimation of long term low resolution surface urban heat island intensities for tropical cities using modis remote sensing data. Urban Clim 17:32–66
Freitas E, Rozoff C, Cotton W, Silva Dias P (2007) Interacions of an urban heat island and sea-breeze circulations during winter over the metropolitan area of São Paulo, Brazil. Boundary-Layer Meteorol 122:43–65
Funari F, Pereira Filho A (2014) Energy balance in a patch of the atlantic forest in São Paulo City. Brazil. J Water Resource Prot 6(805):812
Garratt JR (1980) Surface influence upon vertical profiles in the atmospheric near-surface layer. Q J R Meteorol Soc 106:803–819
Gatunya Ganbat, Jong-Jin Baik, Young-Hee Ryu (2015) A numerical study of the interactions of urban breeze circulation with mountain slope winds. Theor Appl Climatol 120:123–135
Grachev A, Fairall C, Bradley E (2000) Convective profile constants revisited. Boundary-Layer Meteorol 83:423–439
Grimmond C, Oke T (1991) An evapotranspiration interception model for urban areas. Water Resour Res 27:1739–1755
Grimmond C, Oke T (1999b) Aerodynamic properties of urban areas derived from analysis of surface form. J Appl Meteorol 38:1262–1292
Heisler GM, Brazel AJ (2010) The urban physical environment: temperature and urban heat islands Chapter 2. In: Aitkenhead-Peterson J, Volder A (eds) Urban Ecosystem Ecology. Agronomy Monograph 55. American Society of Agronomy, Crop Science Society of America, Soil Science Society of America, Madison, WI, pp 29–56
Hidalgo Nunes L, Koga Vicente A, Henrique Candido D (2015) Tempo e Clima no Brasil - Clima da Regio Sudeste do Brasil, segunda edn. Oficina de textos
IBGE (2008) Instituto brasileiro de geografia e estatística. http://www.ibge.gov.br
Innocentini V (1981) Simulação numérica da brisa marítima: teste de sensibilidade e efeito de parametrizações de transportes turbulentos. Dissertação de mestrado IAG USP São Paulo 1:1–61
Jacquemin B, Noilhan J (1990) Sensitivity study and validation of a land surface parameterization using the hapex-mobilhy data set. Boundary-Layer Meteorol 52:93–134
Kain JS, Fritsch JM (1993) Convective parameterization for mesoscale models: the kain fritsch scheme. In: Emanuel KA, Raymond DJ (eds) The representation of cumulus convection in numerical models. Meteorological Monographs. American Meteorological Society, Boston, MA
Karam H, Oliveira A, Soares J (2003) Application of mass conservation method to investigate the wind patterns over an area of complex topography. J Braz Soc Mech Sci Eng 25:115–121
Karam H, Pereira Filho A, Masson V, Noilhan J, Marques Filho E (2010) Formulation of a tropical town energy budget (t-TEB) scheme. Theor Appl Climatol 101:109–120
Kastner-Klein P, Rotach M (2003) Mean flow and turbulence characteristics in an urban roughness sublayer. Boundary-Layer Meteorol 111:55–84
Kusaka H, Kondo H, Kikegawa Y, Kimura F (2001) A simple single-layer urban canopy model for atmospheric models: comparison with multi-layer and slab models. Boundary-Layer Meteorol 101:329–358
Lei M, Niyogi D, Kishtawal C, Pielke R, Beltrán-Przekurat A, Nobis T, Vaidya S (2008) Effect of explicit urban land surface representation on the simulation of the 26 July 2005 heavy rain event over mumbai, india. Atmos Chem Phys 8:5975–5995
Martilli A, Clappier A, Rotach M (2002) An urban surface exchange parameterization for mesoscale models. Boundary-Layer Meteorol 104:261–304
Mascart P, Noilhan J, Giordani H (1995) A modified parameterization of flux-profile relationship in the surface layer using different roughness length values for heat and momentum. Boundary-Layer Meteorol 72:331–344

Masson V (2000) A physically-based scheme for the urban energy budget in atmospheric models. Boundary-Layer Meteorol 94(357):397
Masson V (2006) Urban surface modeling and the meso-scale impact of cities. Theor Appl Climatol 84:35–45
Melas D, Lavagnini A, Sempreviva A (2000) An investigation of the boundary layer dynamics of sardinia island under sea-breeze conditions. J Appl Meteorol 39:516–524
Miller S, Keim B, Talbot R, Mao H (2003) Sea breeze: structure, forecasting and impacts. Rev Geophys 41:1–31
Moonena P, Gromkec C, Dorera V (2013) Performance assessment of large eddy simulation (LES) for modeling dispersion in an urban street canyon with tree planting. Atmos Environ 75:66–76
Noilhan J (1981) A model for the net total radiation flux at the surfaces of a building. Build Environ 16(4):259–266
Noilhan J, Planton S (1989) A simple parameterization of land surface processes for meteorological models. Mon Weather Rev 117:536–549
Nunez M, Oke T (1976) Long-wave radiative flux divergence and nocturnal cooling of the urban atmosphere within an urban canyon. Boundary-Layer Meteorol 10:121–135
Oke T (1976) The distinction between canopy and boundary-layer urban heat islands. Atmosphere 14:268–277
Oke T (1987) Boundary layer climates, 1st edn. Taylor and Francis Group, London
Oliveira de Souza D, dos Santos Alval R, Guedes do Nascimento M, (2016) Urbanization effects on the microclimate of manaus: a modeling study. Atmos Res 167:237–248
Pearlmutter D, Berliner P, Shaviv E (2005) Evaluation of urban surface energy fluxes using an open-air scale model. J Appl Meteorol 44:532–545
Pereira Filho A, Barros M, Hallak R, Gandu A (2004) Enchentes na região metropilitana de são paulo: aspectos de mesoescala e avaliação de impactos. XIII Congresso Brasileiro de Meterologia, Fortaleza, CE, 28 de Agosto a 03 de Setembro, 2004
Pielke R, Cotton W, Walko R (1992) A comprehensive meteorological modelling system—RAMS. Meteorol Atmos Phys 49:69–91
Ram K, Singh S, Sarin MM, Srivastava AK, Tripathi SN (2016) Variability in aerosol optical properties over an urban site, kanpur, in the indo-gangetic plain: a case study of haze and dust events. Atmos Res 174–175:52–61
Ribeiro F, Soares J, Oliveira A (2016) Sea-breeze and topographic influences on the planetary boundary layer in the coastal upwelling area of Cabo Frio (Brazil). Boundary-Layer Meteorol 158:139–150
Rotach M (1995) Profiles of turbulence statistics in and above and urban street canyon. Atmos Environ 29(13):1473–1486
Schultz P (1995) An explicit cloud physics paramterization for operational numerical weather prediction. Mon Weather Rev 123:3331–3343
Simpson JE (1994) Sea breeze and local wind, 1st edn. Cambridge University Press, Cambridge
Simpson JE (1996) Diurnal changes in sea-breeze direction. J Appl Meteorol 35:1166–1169
Streutker D (2002) Satellite-measured growth of the urban heat island of Houston, Texas. Int J Remote Sens 23:2595–2608
Synnefa A, Santamouris M, Apostolakis K (2007) On the development, optical properties and thermal performance of cool colored coatings for the urban environment. Solar Energy 81:488–497
Tarifa J, Azevedo T (2001) Os climas na cidade de São Paulo: teoría e prática, primeira edn. GEOUSP, Coleção Novos Caminhos
Taylor P (1977) Numerical studies of neutrally stratified planetary boundary-layer flow above gentle topography. I. Two dimensional cases. Boundary-layer Meteorol 12:37–60
Urano A, Ichinose T, Hanaki K (1999) Thermal environment simulation for three dimensional replacement of urban activity. J Wind Eng 81:197–210
Vemado F, Pereira Filho A (2016) Severe weather caused by heat island and sea breeze effects in the metropolitan area of São Paulo. Brazil. Adv Meteorol 8364:134
Voogt J, Grimmond C (2000) Modeling surface sensible heat flux using surface radiative temperatures in a simple urban area. J Appl Meteorol 39:1679–1699
Wan Z (1999) Modis land-surface temperature algorithm theoretical basis document. NASA Documents 3.3, URL http://modis.gsfc.nasa.gov/atbd/atbd-mod11.pdf
Wan Z, Li Z (1997) A physics-based algorithm for retrieving land surface temperature from space. Trans Geosci Remote Sens 34:892–905
Wang X, Parrish D, Kleist D, Whitaker J (2013) GSI 3Dvar-based ensemblevariational hybrid data assimilation for NCEP global forecast system: single-resolution experiments. Mon Weather Rev 141:4098–4117
Xue M, Droegemeier K, Wong V, Shapiro A, Brewster K (2000a) Advanced regional prediction system (ARPS) version 5.3.4 user's guide. Center for Analysis and Prediction of Storms (CAPS), University of Oklahoma, pp 320

Xue M, Droegmeier K, Wong V (2000b) The advanced regional prediction system (ARPS)–a multi-scale nonhydrostatic atmospheric simulation and prediction model. Part I: Model dynamics and verification. Meteorol Atmos Phys 1:1–45

Xue M, Droegmeier K, Wong V (2001) The advanced regional prediction system (ARPS)–a multi-scale nonhydrostatic atmospheric simulation and prediction model. Part II: Model physics and applications. Meteorol Atmos Phys 76:143–165

Yamada T (2000) Building and terrain effects in a mesoscale model. In: 11th Conference on the applications of air pollution meteorology with A&WMA, 9–14 January, Long Beach, CA, vol 1, pp 215–200